Lifetime Prediction of Single Crystal Nickel-Based Superalloys

Ça Gatay Kasar, Utku Kaftancioglu, Emin Bayraktar, Ozgur Aslan

applied sciences

MDPI

Article

Lifetime Prediction of Single Crystal Nickel-Based Superalloys

Çağatay Kasar [1,2,†], Utku Kaftancioglu [2,†], Emin Bayraktar [3,*] and Ozgur Aslan [2,4,*]

[1] Turkish Aerospace Industries, Inc., 06980 Ankara, Turkey; cagatay.kasar@tai.com.tr
[2] Department of Mechanical Engineering, Atılım University, 06830 Ankara, Turkey; kaftancioglu.utku@student.atilim.edu.tr
[3] School of Mechanical and Manufacturing Engineering, ISAE-Supmeca-Paris, Saint Ouen, 93407 Paris, France
[4] Department of Engineering Science, University of Oxford, Oxford OX1 3PJ, UK
* Correspondence: emin.bayraktar@isae-supmeca.fr (E.B.); ozgur.aslan@eng.ox.ac.uk (O.A.)
† These authors contributed equally to this work.

Abstract: Single crystal nickel-based superalloys are extensively used in turbine blade applications due to their superior creep resistance compared to their polycrystalline counterparts. With the high creep resistance, high cycle fatigue (HCF) and low cycle fatigue (LCF) become primary failure mechanisms for such applications. This study investigates the fatigue life prediction of CMSX-4 using a combination of crystal plasticity and lifetime assessment models. The constitutive crystal plasticity model simulates the anisotropic, rate-dependent deformation behavior of CMSX-4, while the modified Chaboche damage model is used for lifetime assessment, focusing on cleavage stresses on active slip planes to include anisotropy. Both qualitative and quantitative data obtained from HCF experiments on single crystal superalloys with notched geometry were used for validation of the model. Furthermore, artificial neural networks (ANNs) were employed to enhance the accuracy of lifetime predictions across varying temperatures by analyzing the fatigue curves obtained from the damage model. The integration of crystal plasticity, damage mechanics, and ANNs resulted in an accurate prediction of fatigue life and crack initiation points under complex loading conditions of single crystals superalloys.

Keywords: crystal plasticity; artificial neural networks; lifetime assessment modelling; turbine blades

Received: 3 October 2024
Revised: 25 December 2024
Accepted: 26 December 2024
Published: 29 December 2024

Citation: Kasar, C.; Kaftancioglu, U.; Bayraktar, E.; Aslan, O. Lifetime Prediction of Single Crystal Nickel-Based Superalloys. *Appl. Sci.* **2025**, *15*, 201. https://doi.org/10.3390/app15010201

1. Introduction

Single crystal nickel-based superalloys are widely preferred in turbine blade components due to their high temperature resistance and mechanical properties [1,2]. Turbine blades are subjected to both severe HCF and LCF loading conditions on top of high operating temperatures, resulting in both fatigue (HCF and LCF) and creep as the main mechanisms of failure [3,4]. Although the presence of creep–fatigue interaction has a negative influence on component life, fatigue fracture is considered to be the main concern of failure in such applications [1,5].

High rotational speed and the fast transient startups of the turbine result in LCF loadings [3]. High-temperature conditions caused by the heated gas inside cause additional creep damage along with LCF loadings [4]. As a result, nickel-based single crystals are often subjected to severe LCF and TMF [6–8]. Understanding the creep–fatigue interaction and LCF fatigue failure of these components is crucial for proper life prediction of such components.

Turbine blades are subjected to vibration loads due to the gas flow within the engine [3,9], resulting in severe HCF loading conditions in addition to LCF and TMF.

Therefore, special attention is paid to HCF lifetime assessment of single crystal superalloys since the reliability and security of aircraft engines are significantly related to the HCF properties of such alloys. In the case of single crystals, crack initiation points and growth directions are highly dependent on the cutting plane and loading types [10,11], unlike most polycrystalline materials. Depending on the crystal structure and operating temperature, plasticity is observed through active slip planes and directions. Although nominal stress is in the elastic region for HCF loadings, plasticity is observed in stress concentration zones as geometric irregularities and micro-cracks. Hence, considering active slip systems is essential to the lifetime assessment of such components.

Fatigue life prediction of single crystal materials is widely investigated from many different aspects. Experimental observations conducted by [12] suggest that for multiaxial cases, fatigue crack initiation and growth occur along dominant slip planes. Based on this phenomenon, many lifetime prediction formulations have been developed with critical plane formulations on probabilistic approaches and modifications to isotropic fatigue formulations to account for multiaxial anisotropy [2,9,13,14], in which resolved shear stresses on the critical planes are chosen as the main concern for failure since it is proven that (being controlled by shear strains) fatigue cracks initiate along crystallographic directions [12]. Once initiated, crack growth is also controlled by the maximum shear strain direction. However, the maximum stress direction of these mechanisms may differ from one another depending on the crystallographic orientations.

Fatigue life prediction methods based on continuum damage mechanics evaluate the damage parameter, D, cycle by cycle, with crack nucleation occurring when the damage reaches a critical level. Early approaches, such as the Palmgren-Miner rule, model damage as a linear function of lifetime, later extended to nonlinear behaviors using models such as Double Linear Damage Rule (DLDR), Damage Curve Approach (DCA), and Double Damage Curve Approach (DDCA) [15]. These methods are commonly paired with stress- or strain-based approaches for lifetime prediction under variable amplitude loading. Chaboche and Lemaitre [16] introduced a nonlinear damage evolution equation incorporating multiaxial loading via equivalent stress amplitudes. Due to its mathematical formulation, the Chaboche model can be readily implemented in computational tools, facilitating its application in complex fatigue analyses. This model is particularly effective for single crystals, aligning with DCA under complex loading and critical slip plane stress formulations, and its mathematical formulation allows for straightforward integration into computational tools, enabling efficient fatigue analysis compared to other approaches [15,17].

Integrating artificial neural networks (ANNs) into fatigue life assessment has significantly enhanced prediction accuracy and efficiency. ANNs are adept at handling complex, nonlinear interactions between variables, which are common in fatigue scenarios. Researchers like Samavatian et al. [18] have demonstrated that machine learning can predict solder joint reliability under cyclic stress with higher precision than traditional methods. Moreover, ANNs have been applied to interpret multiaxial fatigue data, offering new insights into the critical stress and strain thresholds that precede material failure [19]. These advancements underscore the potential of ANNs to refine predictive models in high-stakes applications such as aerospace engineering, where many material failure mechanisms occurs simultaneously.

In this study, the fatigue life of CMSX-4 is predicted, initially, by considering both crystal plasticity and multiaxial fatigue properties. The small strain constitutive crystal plasticity model, described later on, is used for modelling the stress–strain behaviour of the single crystal on geometric irregularities. Lifetime assessment modelling is conducted on the stress history obtained from the single crystal model by considering the cleavage

stress as the main failure. Parameter optimization is performed for the Chaboche model at three different temperatures, and the fatigue curves provided by these models are fed into ANNs, where lifetime assessment is conducted for different temperatures with a single optimized model, unlike the Chaboche model.

2. Experimental Procedure and Methodology

HCF test results and notched specimen geometry were taken from Aslan [10], in which CMSX-4 specimen preparation procedures and various tensile and fatigue tests at different R ratios are widely discussed, provided by the PREMECCY project. Testing protocols, such as specimen preparation, environmental conditions, and failure criteria, are provided in detail in [10]. The notched specimen geometry and cyclic loading amplitudes were used to simulate the experimental results and to model the material behavior. Specific details related to the modeling approach are discussed in the following sections.

2.1. Material and Specimen

Second generation nickel-based single crystal superalloy CMSX-4, whose chemical composition (in wt%) is presented in Table 1, was solution treated below and rapidly cooled to achieve a high volume fraction of γ' precipitates (around 70%), which is the prime strengthening phase in the material.

Table 1. Chemical Composition of CMSX-4 (wt%).

Ni	Cr	Co	Mo	W	Al	Ti	Ta	Re	Hf
61.8	6.5	9	0.6	6	5.6	1	6.5	3	0.1

Notched specimens with a cut orientation of (100)[001] are subjected to cyclic tension for R = 0 and R = 0.6 with a frequency of 118 Hz at 750 °C. Figure 1 demonstrates the dimensions of the notched specimen with a 1.6 mm notched thickness. The presence of a notched area leads to varying stress concentrations depending on the notch radius and thickness. Therefore, relating lifetime to the maximum stress at the specimen's notch, rather than the applied stress, provides a more generalized understanding of fracture behaviour.

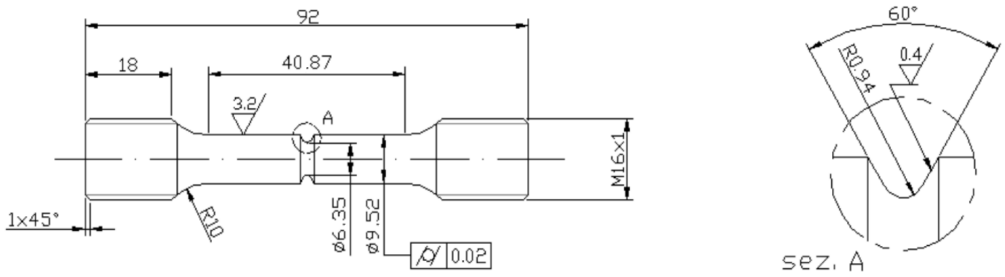

Figure 1. Dimensions of the notched specimen.

The elastic stress concentration factor, K_t, is determined as 2.15 for the geometry represented in Figure 1 and the stress at the notched tip, σ_{max} is calculated by

$$\sigma_{max} = K_t \, \sigma_{nom} \tag{1}$$

where σ_{nom} is the nominal stress across cross-section of the specimen.

2.2. Crystal Plasticity

The constitutive framework of the single-crystal plasticity model, developed from Cailletaud's crystallographic model [20], is presented in this section. This formulation

primarily operates at mesoscales (10^{-7} m to 10^{-4} m) by modeling the dislocation motion and latent interaction within the slip systems. At this scale, formulation captures the localized plastic strains on active slip systems. The formulation does not directly predict the macro-strain response of the material; however, the accumulation of micro-strains on active slip systems, depending on the orientation of the material and the orientation of the loading, averages the overall response of the material and hence gives the macro-response of the stress–strain distribution [21]. This model was prepared to simulate the anisotropic rate-dependent plastic behaviour of Ni-based superalloys at small strains. The linear strain tensor can be shown as $\boldsymbol{\varepsilon} = sym[\nabla \mathbf{u}]$ from the definition of the symmetric part of the displacement gradient, and since small deformation is used in this work, an additive decomposition is applied.

$$\boldsymbol{\varepsilon} = \boldsymbol{\varepsilon}^e + \boldsymbol{\varepsilon}^p \tag{2}$$

where $\boldsymbol{\varepsilon}^e$ is the elastic strain and $\boldsymbol{\varepsilon}^p$ is the plastic part. The relationship between Cauchy stress, $\boldsymbol{\sigma}$, and elastic strain is expressed as a state law as follows:

$$\boldsymbol{\sigma} = \mathbf{C} : \boldsymbol{\varepsilon}^e \tag{3}$$

where $\mathbf{C}$ is the fourth order elasticity moduli. Material to be simulated has an FCC structure. It shows cubic elastic behavior. Hence, $\mathbf{C}$ has 3 independent constants, $\mathbf{C_{11}}$, $\mathbf{C_{12}}$, and $\mathbf{C_{44}}$, as can be seen below.

$$\mathbf{C} = \begin{bmatrix} C_{11} & C_{12} & C_{12} & 0 & 0 & 0 \\ C_{12} & C_{11} & C_{12} & 0 & 0 & 0 \\ C_{12} & C_{12} & C_{11} & 0 & 0 & 0 \\ 0 & 0 & 0 & C_{44} & 0 & 0 \\ 0 & 0 & 0 & 0 & C_{44} & 0 \\ 0 & 0 & 0 & 0 & 0 & C_{44} \end{bmatrix} \quad \text{where} \quad \begin{aligned} C_{11} &= \frac{1}{3}(3K + 4\mu) \\ C_{12} &= \frac{1}{3}(3K - 2\mu) \\ C_{44} &= \mu + \mu' \end{aligned} \tag{4}$$

where K is bulk modulus, μ is shear modulus and μ' is the effective shear modulus describing shear resistance in specific crystallographic directions [22]. Another state law can shown which represents isotropic hardening of the each slip system as:

$$r^s = q \sum_{s=1}^{N} h^{sr} \rho^s \tag{5}$$

where q is a material constant defining isotropic hardening, s is the slip system, and N is the total number of slip systems. h^{sr} is the interaction matrix that governs the self and latent hardening of the material caused by the interactions between the N number of slip systems. Literature usually suggests taking h^{sr} as the identity for single crystal Ni-based superalloys since they do not show pro-dominant latent hardening [23]. And ρ^s is the dislocation density, which can be defined as a nonlinear isotropic hardening rule as

$$\rho^s = 1 - exp(-b|\gamma^s|) \tag{6}$$

where b is a model parameter; hence, r^s becomes

$$r^s = q \sum_{s=1}^{N} (1 - exp(-b|\gamma^s|)) \tag{7}$$

In order to define γ^s (which is plastic slip of slip system s), Schmid law must be presented here:

$$f^s = |\tau^s| - r^s \tag{8}$$

where τ^s is the resolved shear stress of slip system s, which is the driving force for the plastic slip of the corresponding slip system. In other words, for a slip system to deform plastically, the resolved shear stress must overcome a stress barrier defined by Schmid law. Hence, Schmid law here can be used as a multimechanism plastic yield criterion. The resolved shear stress can be calculated as

$$\tau^s = \sigma : (\mathbf{m}^s \otimes \mathbf{n}^s) \tag{9}$$

where $\mathbf{m}^s$ is the slip direction of slip system s and $\mathbf{n}^s$ is the corresponding slip normal. Table 2 shows a list of slip normals and directions of FCC materials.

Table 2. FCC crystal slip system list.

Slip System Family	System s	Slip Normal $\mathbf{n}^s$	Slip Direction $\mathbf{m}^s$
Octahedral	1	(111)	$[\bar{1}01]$
	2		$[0\bar{1}1]$
	3		$[\bar{1}10]$
	4	$(1\bar{1}1)$	$[\bar{1}01]$
	5		[011]
	6		[110]
	7	$(\bar{1}11)$	$[0\bar{1}1]$
	8		[110]
	9		[101]
	10	$(11\bar{1})$	$[\bar{1}10]$
	11		[101]
	12		[011]
Cubic	1	(001)	$[\bar{1}10]$
	2		[110]
	3	(100)	[011]
	4		$[0\bar{1}1]$
	5	(010)	$[\bar{1}01]$
	6		[101]

Then, according to the maximum energy dissipation principle, plastic strain rate can be written as

$$\dot{\boldsymbol{\epsilon}}^{\boldsymbol{p}} = \sum_{s=1}^{N} \dot{\gamma}^s (\mathbf{m}^s \otimes \mathbf{n}^s) \tag{10}$$

where finally, plastic slip rate of slip system s can be defined using a Norton rule with a threshold as

$$\dot{\gamma}^s = \langle \frac{|\tau^s| - r^s}{K} \rangle^n \, sign(\tau^s - r^s) \tag{11}$$

where K here behaves as a plastic slip threshold and n is the rate-sensitivity parameter.

2.3. Lifetime Assessment

2.3.1. Critical Stress Determination

Selecting an equivalent stress that accounts for material and loading type specifics is crucial for accurate life estimations, especially for complex geometries, such as those involving triaxialty. For most metals, maximum principle stress and von Mises stress are considered to be the correct approach for estimating multiaxial fatigue. For single crystals, however, it is better to include the slip planes to cover the anisotropic response of every possible cut orientation of single crystals.

FCC single crystals have four active octahedral slip planes and three active cubic slip planes, as presented in Figure 2a,b. The effect of cubic slip systems is observed at elevated temperatures due to a higher activation energy requirement for plasticity, while octahedral systems are active even at room temperature, thanks to their densely packed structure. Motivated by the fact that fracture occurs on active slip planes, stress along cleavage stress directions is determined to be the deciding factor for fatigue life estimations.

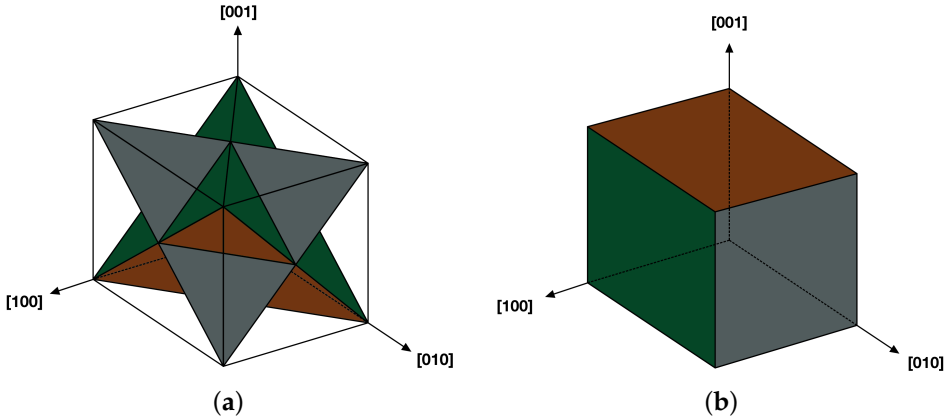

Figure 2. Octahedral (**a**) and cubic (**b**) slip planes of a FCC crystal.

Experimental studies show that mixed-mode loadings are apparent in multi-axial fatigue fractures for many different specimens and loading types. Figure 3 illustrates the crack opening modes, with cleavage systems referred to as Mode I, and accommodation systems as Modes II and III. Mode I is observed to be the most dominant among the other modes, even under pure shear loadings, since the appearance of shearing and tearing modes of the crack is observed to be dependent on crack incline and material orientation. The cleavage system is always present, and the accommodation systems are observed to be dependent on fatigue loadings. The growth of fatigue micro-cracks is under the influence of the cleavage system more than the others [24–27]. Under these findings, critical stress is chosen to be the cleavage stresses acting on the slip planes where cracks are initiated.

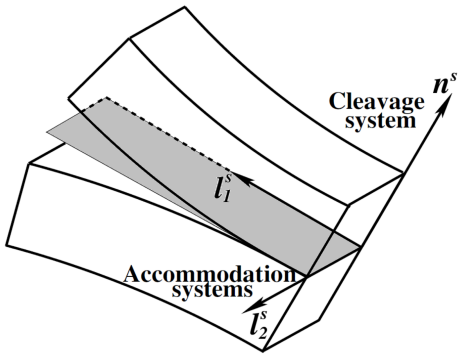

Figure 3. Demonstration of opening modes of a crack.

2.3.2. Modified Fatigue Damage Law

Damage law is generally expressed by assuming that the fatigue damage accumulated at each cycle is a function of the amplitude and mean values of stress:

$$\delta D = f(\sigma_{amp}, \sigma_{mean})\, \delta N \tag{12}$$

where D is the scalar variable representing fatigue damage evolution from the virgin state ($D = 0$) up to fatigue fracture ($D = 1$). Lemaitre and Chaboche [16] proposed fatigue life models based on the Woehler rule for both uniaxial and multiaxial cases. Multiaxial fatigue

damage is estimated by using equivalent fatigue limit and stress values relevant to the loading conditions. Due to the anisotropic nature of single crystals, the crack initiation location and propagation path occur specific to the slip systems of the material. Since the consideration of both crack initiation and propagation is essential for the fatigue lifetime assessment of single crystals, the cleavage stress acting on the crack is considered instead of the macroscopic equivalent amplitude stress. The differential equation of the fatigue damage on the dominant cleavage plane is expressed as:

$$\delta D^{clv} = \left[1-(1-D)^{\beta+1}\right]^{\alpha(\sigma^{clv}_{amp},\,\sigma^{clv}_{mean})} \left[\frac{\sigma^{clv}_{amp}}{M(\sigma^{clv}_{mean})(1-D)}\right]^{\beta} \delta N \tag{13}$$

where σ^{clv}_{amp} and σ^{clv}_{mean} are the dominant cleavage stress amplitude and mean stress, respectively, and β is a temperature-dependent model parameter. The function α represents the effects of nonlinear accumulation:

$$\alpha(\sigma^{clv}_{amp},\,\sigma^{clv}_{mean}) = 1 - a\left\langle \frac{\sigma^{clv}_{amp} - \sigma_l(\sigma^{clv}_{mean})}{\sigma^{clv}_{uts} - \sigma^{clv}_{max}} \right\rangle \tag{14}$$

where a is a model parameter, σ_{uts} is the ultimate tensile stress, and σ_l is the fatigue limit in terms of amplitude stress. The relation between fatigue limit and mean stress is represented by Goodman's linear relation:

$$\sigma^{clv}_{l} = \sigma^{clv}_{l_0}(1 - b_1\sigma^{clv}_{mean}) \tag{15}$$

where σ_{l_0} is the fatigue limit at zero mean stress i.e., endurance limit, and b_1 is the model parameter establishing the relation between fatigue limit and mean stress. M is expressed with the same linear relation dependent on mean stress and model parameters b_2 and M_0 as

$$M = M_0(1 - b_2\sigma^{clv}_{mean}) \tag{16}$$

Fatigue life, N_f, of a material is determined by integrating the damage variable, D, in Equation (13) from 0 to 1 since $D = 1$ represents the fatigue failure of a virgin material.

$$N_f = \frac{1}{(\beta+1)[1-\alpha(\sigma^{clv}_{amp},\,\sigma^{clv}_{mean})]} \left[\frac{\sigma^{clv}_{amp}}{M(\sigma^{clv}_{mean})}\right]^{-\beta} \tag{17}$$

2.3.3. Artificial Neural Networks (ANNs)

ANNs are machine learning tools designed to establish the nonlinear relation between the given input and the desired output by imitating the human brain's neurological structure [28]. ANNs are composed of three main parts, as demonstrated in Figure 4.

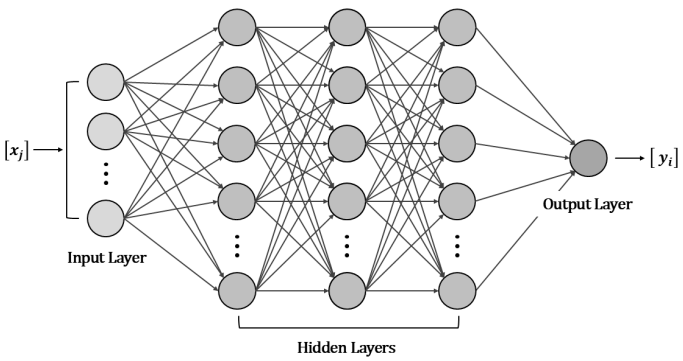

Figure 4. Structure of artificial neural networks designed for regression tasks, demonstrating input, hidden, and output layers.

The input vector, x_j, represents the independent variables affecting the output vector, y_i. Hidden layers are used for establishing the nonlinear relationship between the input layer and the output layer. Hidden layers receive different independent variables from the input layer and modify this information by adjusting weights, w_{ij} and biases b_i. The mathematical notation of the i-th neuron in a hidden layer as follows

$$y_i = g_i\left(\sum_j w_{ij}x_j + b_i\right) \tag{18}$$

The activation function, g_i, introduces the nonlinearity to the system by processing the established linear relation by weights and biases. These functions are one of the main parameters used to control the output range and learning ability of artificial neurons. Since ANNs are built up in a feed-forward structure, the output produced from each neuron feeds into the next neuron until the prediction in the output neuron is established. The adjustment of weights and biases is performed by monitoring the output difference between the predicted and actual outcome using the backward propagation algorithm: gradient descent . ReLUs, demonstrated in Equation (19), are preferred in many cases as activation functions since they reduce the vanishing gradient problem and its derivatives are easier to compute. In the vanishing gradient problem, gradients tend to get smaller as the training progresses, slowing down the learning significantly or completely terminating it.

$$ReLU(x) = max(0, x)\ i.e.,\ \left\{\begin{array}{ll} x, & \text{if } x > 0 \\ 0, & \text{if } x \leq 0 \end{array}\right\} \tag{19}$$

The difference between the actual output and predicted values in the output layers is computed by establishing a loss function, L, between the two, such as mean square error. The loss function is minimized by taking its derivatives with respect to weights and biases in each iteration, k, until an acceptable error between predicted and actual data is achieved. The mathematical expression of the loss function optimization, i.e., gradient descent as follows:

$$b_i^{k+1} = b_i^k - \alpha\frac{\partial L}{\partial b_i^k} \tag{20}$$

$$w_{ij}^{k+1} = w_{ij}^k - \alpha\frac{\partial L}{\partial w_i j^k} \tag{21}$$

Convergence to the minimum value of the loss function is controlled by the learning rate value, α, which acts like the step size between each iteration.

2.3.4. Finite Element Model of the Nothced Specimen

The finite element model of the notched specimen presented in Figure 1 is created via Abaqus/CAE 2018 by using quadratic axisymmetric elements (CAX8), and the corresponding FEA mesh of the specimen is presented in Figure 5a. Single crystal material behaviour is implemented using the small strain crystal plasticity theory described in Section 2.2 as a user material subroutine (UMAT).

Concerning mesh sensitivity, rate dependency smooths deformation gradients, helping prevent the sharp localizations often observed in elasto-plastic models. This effect, along with the absence of softening behavior, which also avoids localization of the plastic field, reduces the model's sensitivity to mesh refinement [29,30].

The boundary conditions applied to the finite element model are as follows: the bottom edge of the specimen is fixed along the y-axis, with the left edge set as a symmetry axis due to the model's axisymmetric geometry. A cyclic force amplitude is applied on the top face to simulate loading conditions, as shown in Figure 5b.

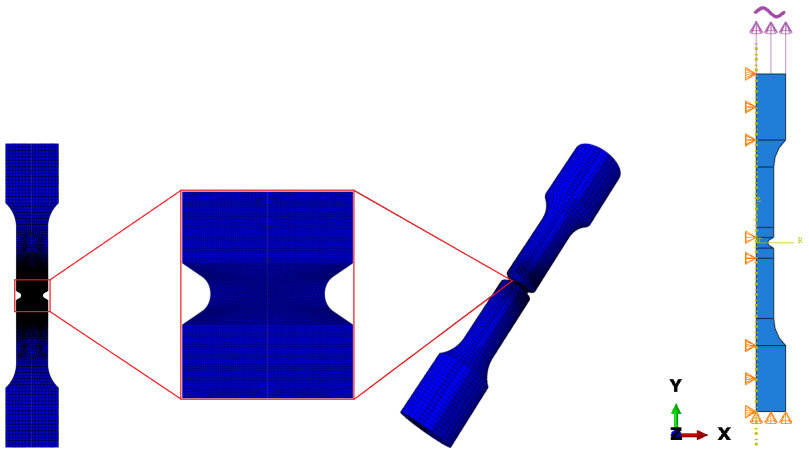

(**a**) (**b**)

Figure 5. Finite element mesh (**a**) and the boundary conditions (**b**) of the notched specimen.

2.3.5. Post-Scripting of Modified Chaboche Model

The stress history at each integration point was obtained from the output database (ODB) of the single crystal plasticity model using Abaqus post-scripting Python 2.7 modules. The process utilized the odbAccess module for accessing ODB data, the abaqusConstants module for specifying data positions such as integration points, and visualization for analyzing the extracted data. Stress tensor components (S, SDV) at all integration points and nodal displacement values (U) were extracted for each frame to obtain the cyclic loading history and nodal positions throughout the analysis.

Based on the stress histories, the peak-valley algorithm was used to determine the maximum and minimum stress values for each cycle. These values were then used to compute the mean and amplitude stresses, which are required inputs for the modified Chaboche model. By applying the multiaxial anisotropic lifetime assessment theory described in Section 2.3.2, the lifetime at each node is estimated. Lifetime values and the mesh information of the FEA model are stored in the visualization toolkit data format (.vtk) to obtain lifetime contours via Paraview, which is an open-source post-processing visualization engine.

2.3.6. ANN Model Configuration

ANNs are made up of 20 hidden layers with 20 neurons and a single output layer and neuron to predict the lifetime. The stochastic gradient descent optimizer "Adam" is used since it adjusts its learning rate with a corresponding decrease in the loss function, and the initial learning rate is set to 0.0001.

Loss function and metric are chosen as Mean Square Error (MSE) and Root Mean Square Error (RMSE), respectively. The training data, formed with the damage model, is consistent and does not contain data points that differ significantly from others, making MSE a suitable loss function for this case. Stress-lifetime values fed into the ANNs are on a logarithmic scale, eliminating the need for a logarithmic error. This yields better training results rather than using actual lifetime values with mean squared logarithmic error (MSLE). Lifetime data ranges from 1 to 10^{10}, and it is normalized before being fed into the input layer. Logarithmic scaling decreases the difference between maximum and minimum lifetime values, thus making it easier for ANNs to compute the nonlinear relation.

$$\text{Loss (MSE)} = \frac{1}{n}\sum_{i=1}^{n}(y_i - \hat{y}_i)^2$$
$$\text{Metric (RMSE)} = \sqrt{\frac{1}{n}\sum_{i=1}^{n}(y_i - \hat{y}_i)^2} \quad \text{where } y_i = \log(N_f)_i \text{ and } \hat{y}_i = \log(\hat{N}_f)_i \tag{22}$$

The dataset is divided into 70% for training, 15% for validation, and 15% for an independent test set. During training, the validation set is used to monitor performance by tracking validation loss and metrics, ensuring the model does not overfit. After training, the independent test set, unseen during training and validation, is evaluated to assess the model's generalization and predictive accuracy on unseen data.

3. Results and Discussion

3.1. Lifetime Prediction of the Notched Specimen at 750 °C

The plastic slip threshold parameter K and the rate sensitivity parameter were chosen to mimic the stress–strain behaviour of CMSX-4 at 750 °C. The elastic moduli constants of CMSX-4 provided in Table 3 were taken from the literature [31].

Table 3. Parameters of crystal plasticity model for CMSX-4.

K (MPa$^{1/n}$)	n	Q	b	C_{11} (GPa)	C_{12} (GPa)	C_{44} (GPa)
2200	7.5	100	250	296	204	125

The temperature-dependent material parameters of the lifetime assessment model, yield strength (σ_{yield}), and ultimate tensile strength (σ_{uts}) of CMSX-4 at 600 °C, 750 °C, and 900 °C were taken from the literature [32]. The amplitude stress and mean stress were calculated from HCF results, and the temperature-dependent model parameters were adjusted for a proper lifetime estimation on both R ratios.

The Table 4 demonstrates the parameter set of both the crystal plasticity and lifetime assessment models. Since CMSX-4 does not exhibit an actual fatigue limit due to its FCC microstructural nature, the endurance limit (σ_{l_0}) was determined to be 0 instead of choosing a specific lifetime as the infinite lifetime and corresponding stresses as the fatigue limit for better visualization of lifetime throughout the specimen. Since fatigue limit computed for different mean stress would also yield zero, the parameter, b_1 becomes obsolete in this case. The remaining parameters were manually fitted to the experimental data, which includes at most two R-ratios per temperature. Optimization algorithms, such as gradient descent or genetic algorithms, were not used as they offered no significant advantage in this case.

Table 4. Parameters of anisotropic lifetime assessment model for CMSX-4.

σ_{uts} (MPa)	σ_{yield} (MPa)	M_0 (MPa)	$\sigma_{l_0}^{clv}$ (MPa)	b_1 (MPa^{-1})	b_2 (MPa^{-1})	a	β
1200	1100	1800	0	1.12×10^{-4}	1.12×10^{-4}	0.65	7.8

The maximum cyclic stress–strain distribution of the CMSX-4 notched specimen with a cut orientation of (100)[001] is represented in Figure 6. Stress on the notch tip remains elastic throughout the whole cyclic loading for R ratios of 0 and 0.6, as observed in HCF loadings. Figure 6 suggests that the maximum applied stress distribution and lifetime distribution differ according to the dominant cleavage stress directions along active slip systems.

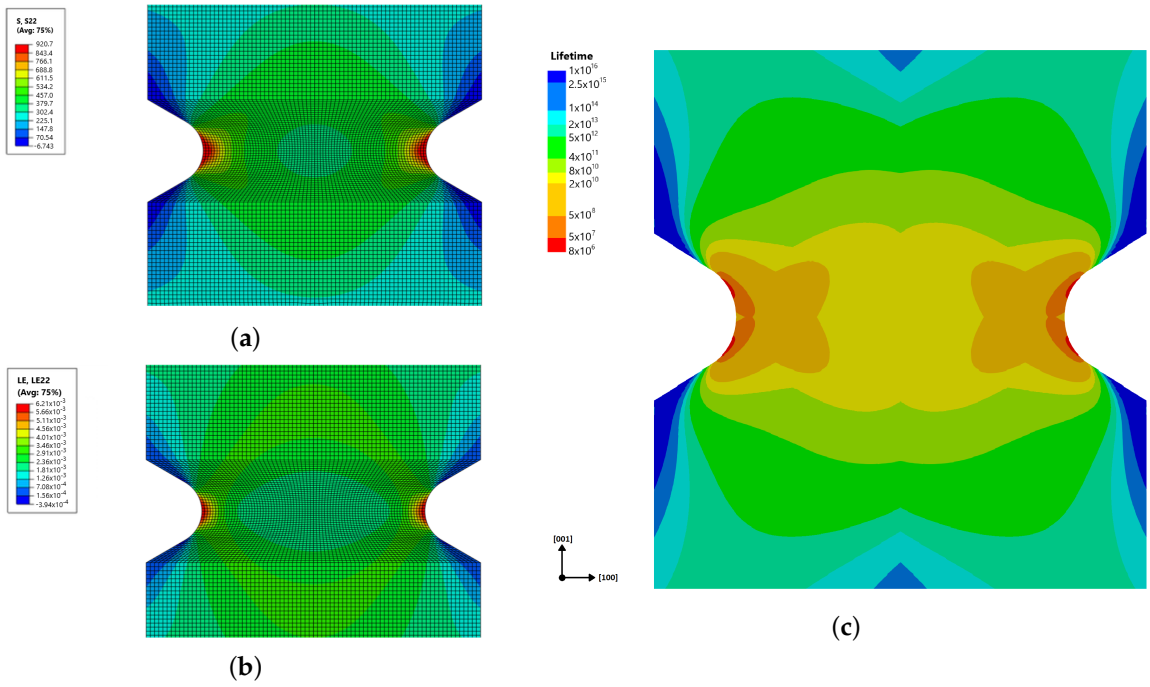

Figure 6. Stress in 22-direction (**a**), logarithmic strain in 22-direction (**b**), and lifetime (**c**) contours of a single crystal notch specimen under HCF with R= 0.6 and cut orientation of (100)[001].

For (100)[001] cut orientation, octahedral slip planes are observed to be more dominant compared to cubic systems, even at elevated temperatures. Therefore, it is only natural to expect crack initiation on {111} planes and crack growth paths along cleavage (Mode I opening) stress directions. As a result, crack initiation points are completely dependent on the orientation of the specimen with the same applied elastic stress distribution as in Figure 6.

Lifetime distributions for different cut orientations are determined by adjusting the local coordinate system of the crystal plasticity model to align with the tensile loading direction. A comparison of crack initiation points with simulation results for different cut orientations of the notch specimen is provided in Figures 7 and 8.

Fatigue crack initiation of the notched specimen with crystal orientation of <001> takes place above the notch tip in spite of the higher geometric stress concentration on the notch tip, as represented in Figure 8a. This result is due to the high accumulation of slip in these regions caused by the elastic and plastic anisotropy of the cut orientation [33]. In Figures 7a and 8c, this phenomenon is observed on the notch tip for <011> and <111> orientations since dominant slip systems provided in Table 2 are along the tensile loading directions.

In Figures 7 and 8, lifetime prediction contours of these cut orientations yield consistent crack initiation points with the experimental results since maximum cleavage stress appears on the slip accumulation regions.

HCF lifetime simulation results of the notched CMSX-4 specimen geometry provided in Figure 1 for different R ratios at 750 °C, with the parameter set in Tables 3 and 4, are provided in Figure 9. Lifetime predictions for both $R = 0$ and $R = 0.6$ are consistent with the experimental results.

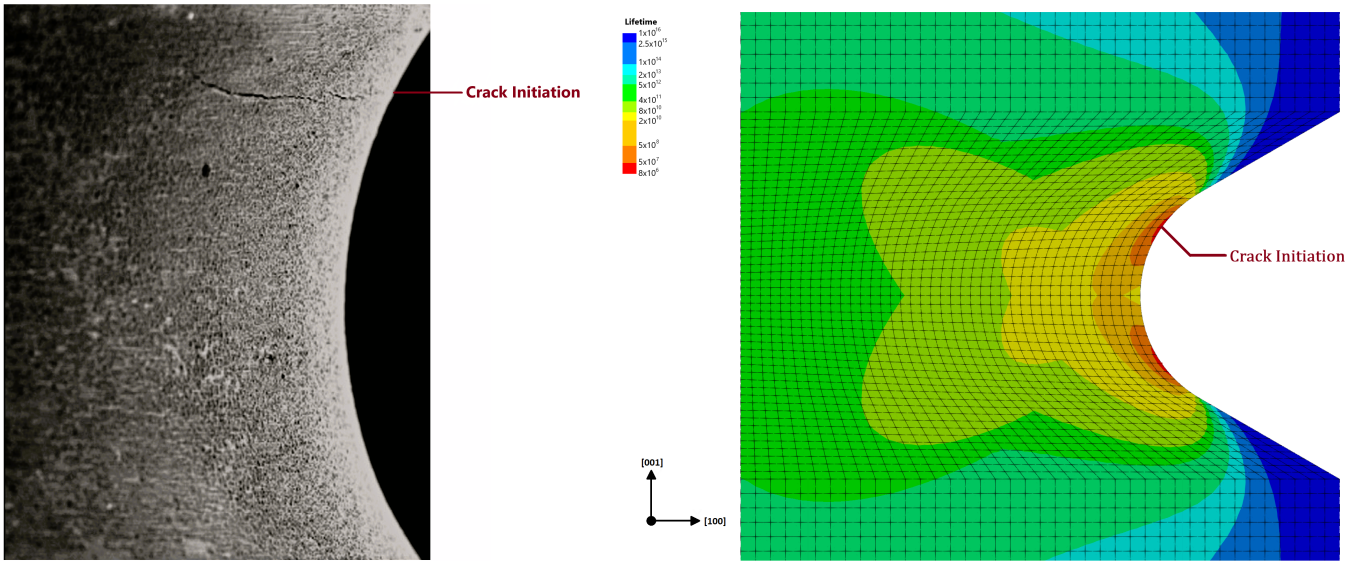

(**a**) (**b**)

Figure 7. Fatigue crack initiation at the surface of SC16 nickel-base single crystal with tensile crystal orientation <001> is represented in (**a**). Reproduced with permission from S. Forest, Crystal plasticity and damage at cracks and notches in nickel-base single-crystal superalloys; published by Elsevier, 2022 [33]. Lifetime assessment of the same specimen orientations is represented in (**b**), where the minimum lifetime on the FEA model is marked as the predicted crack initiation location.

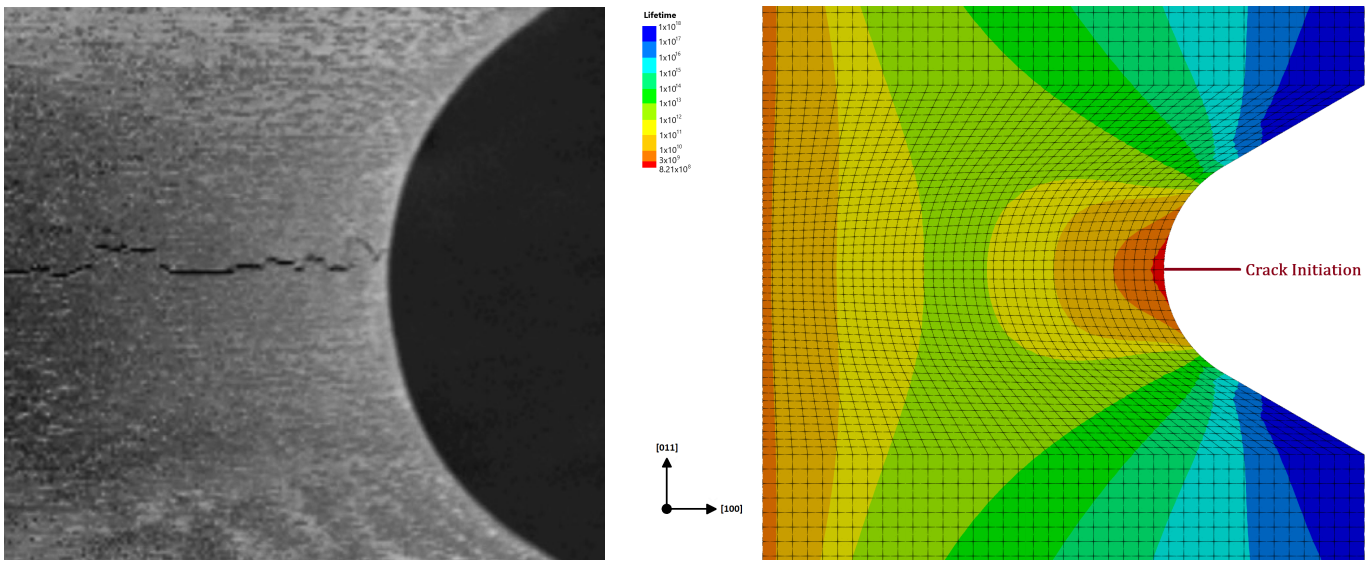

(**a**) (**b**)

Figure 8. *Cont.*

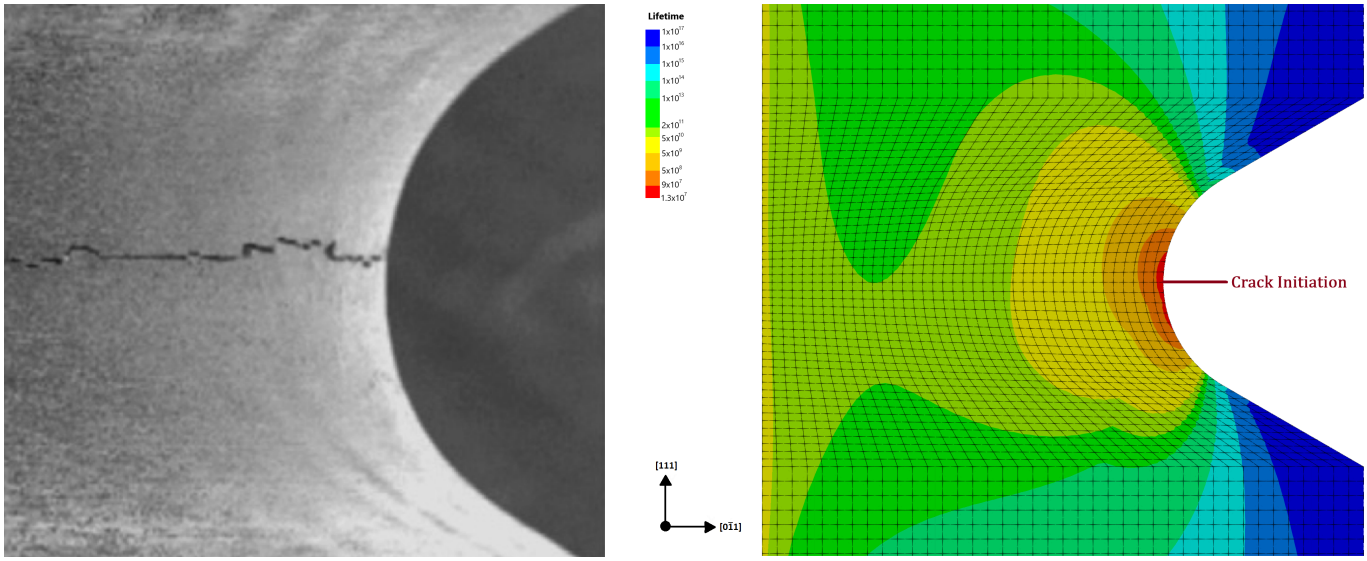

(**c**) (**d**)

Figure 8. Fatigue crack initiation at the surface of SC16 nickel-base single crystal with tensile crystal orientations <011> and <111> are represented in (**a**,**c**). Reproduced with permission from S. Forest, crystal plasticity and damage at cracks and notches in nickel-base single-crystal superalloys; published by Elsevier, 2022 [33]. Lifetime assessment of the same specimen orientations is represented in (**b**,**d**), respectively, in which the minimum lifetime on the FEA model is marked as the predicted crack initiation location.

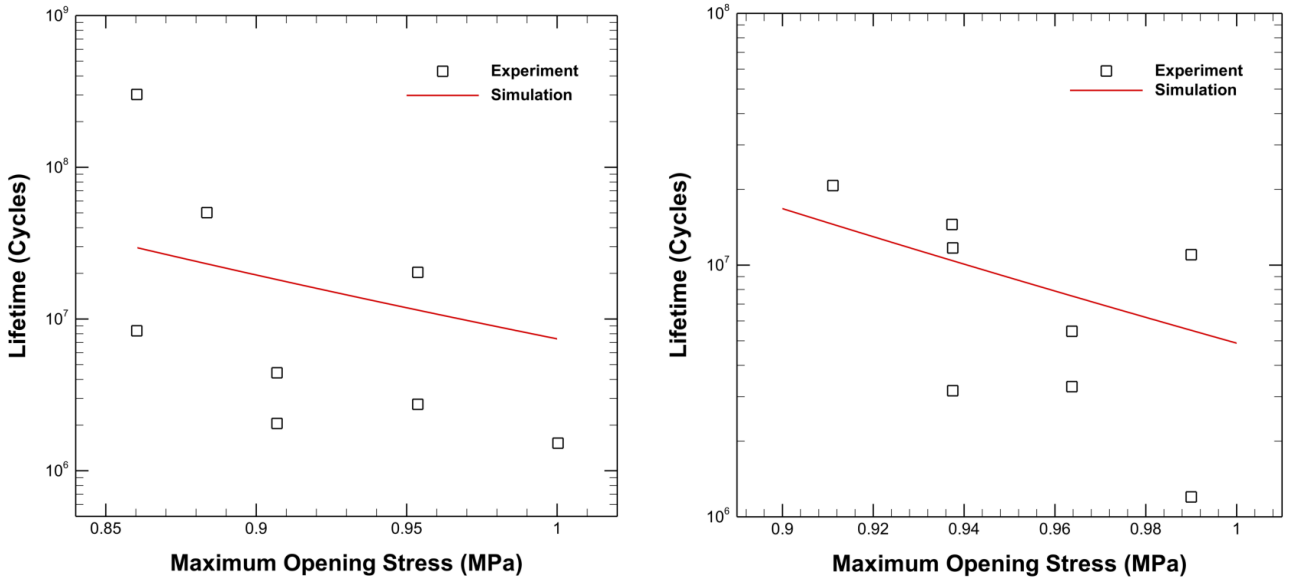

(**a**) (**b**)

Figure 9. Comparison of numerical and experimental results of CMSX4 notched specimen under HCF loading at 750 °C with R = 0 (**a**) and R = 0.6 (**b**).

3.2. Fatigue Curve Predictions with Artificial Neural Networks

Training Dataset Configuration

The temperature-dependent material parameter of the lifetime assessment model, ultimate tensile strength (σ_{uts}) of CMSX-4 at 600 °C and 900 °C, was taken from the literature [32]. This parameter also serves as model input, and parameter optimization was performed separately for each temperature, as represented in Table 5. Fatigue curves at these temperatures are producible with the damage model; however, this temperature

dependency makes it impossible to predict temperature variation without making further modifications to the damage law. Artificial neural networks (ANNs) do not have this restriction since temperature is another variable to establish the nonlinear relation between input variable maximum stress, R ratio, and output variable lifetime result.

Table 5. Parameters of modified damage model of CMSX-4 for various temperatures.

T (°C)	σ_{uts}^{clv} (MPa)	M_0 (MPa)	$\sigma_{l_0}^{clv}$ (MPa)	b_1 (MPa^{-1})	b_2 (MPa^{-1})	a	β
600	840	1010	480	1.24×10^{-3}	1.22×10^{-3}	0.01	14.5
900	675	800	375	2.2×10^{-3}	1.15×10^{-3}	0.12	12.2

ANNs require a wide range of loading information at these temperatures to accurately predict the lifetime of components under complex loadings. Since producing experimental results for single crystal superalloys such as CMSX-4 is not feasible, the combination of ANNs and the modified damage model enhances the performance of both approaches in lifetime assessment by providing the data range from the damage model and making predictions without parameter restrictions with ANNs. The parameter optimization of the modified damage model for 600 °C and 900 °C is demonstrated in Table 5. Although FCC materials do not generally demonstrate a clear fatigue limit, for this case, a target lifetime of 10^8 is considered as infinite life; the fatigue limit is adjusted by defining σ_{l_0} as the endurance limit for $R = -1$ and establishing the relation between mean stress and fatigue limit with parameter, b_1.

Fatigue curves produced by Chaboche Model for 600 °C and 900 °C with R ratios from 0 to 0.4 are fed into ANNs to achieve temperature variance between 600 °C and 900 °C. These curves are illustrated in Figure 10.

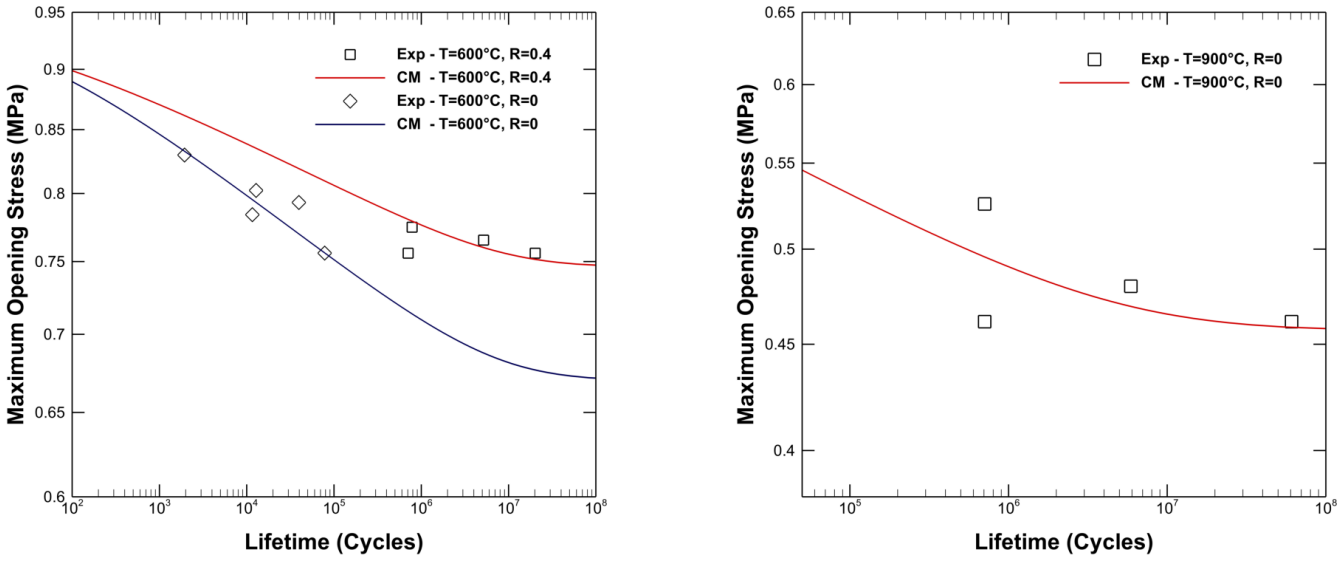

(**a**) (**b**)

Figure 10. Comparison of modified Chaboche model (CM) and experimental results of CMSX4 at 600 °C for R = 0 and R = 0.4 (**a**) and at 900 °C for R = 0 (**b**).

RMSE of training and validation set are monitored during training and RMSE of independent test set is evaluated to assess the general behavior of the model. In addition to this evaluation, mean absolute error (MAE) and R^2 score for both sets are also evaluated to address the model's predictive accuracy.

Since the evaluated lifetime values are in the log_{10}-domain, translating the errors, represented in Table 6, back to the original scale results in multiplicative factors for the validation and independent test sets of 1.419 and 1.429 for MAE, and 1.822, and 1.845 for RMSE, respectively. Small MAE and RMSE values in the log_{10}-domain correspond to reasonable multiplicative errors in the original domain, making the model reliable for practical fatigue life prediction. The high R^2 score highlights the model's reliability and strong correspondence with the underlying data.

Table 6. Performance metrics of the model on validation and independent test sets.

Dataset	RMSE	MAE	R^2
Validation Set	0.2605	0.1521	0.9919
Independent Test Set	0.2659	0.1549	0.9902

Fatigue curves produced on the training data spectrum, Figure 11, demonstrate that it is possible to reproduce the lifetime results obtained by modified Chaboche models with two different parameter sets using ANNs. The smooth data flow suggests that training performed with a batch size of 3.5% of the training data for 250 epochs provides sufficient data to establish the effects of fatigue limit and temperature, as well as the convergence to ultimate tensile strength for each R ratio at the same temperature, without over-training the model.

The uncertainty analysis indicates that the model performs reliably under small (1%) and moderate (5%) perturbations, resulting in multiplicative uncertainties of approximately 1.3 and 3.5, respectively, for both validation and test datasets, as represented in Table 7. These findings suggest that the model maintains consistent predictions within the trained input range. For larger perturbations (10%), however, the uncertainty increases significantly, highlighting the model's sensitivity to inputs beyond the training data distribution.

Table 7. Average uncertainty (standard deviation) for validation and test datasets under different input perturbations.

Perturbation Level (%)	Validation SD	Test SD
1%	0.1269	0.1106
5%	0.5397	0.5158
10%	0.9812	0.9581

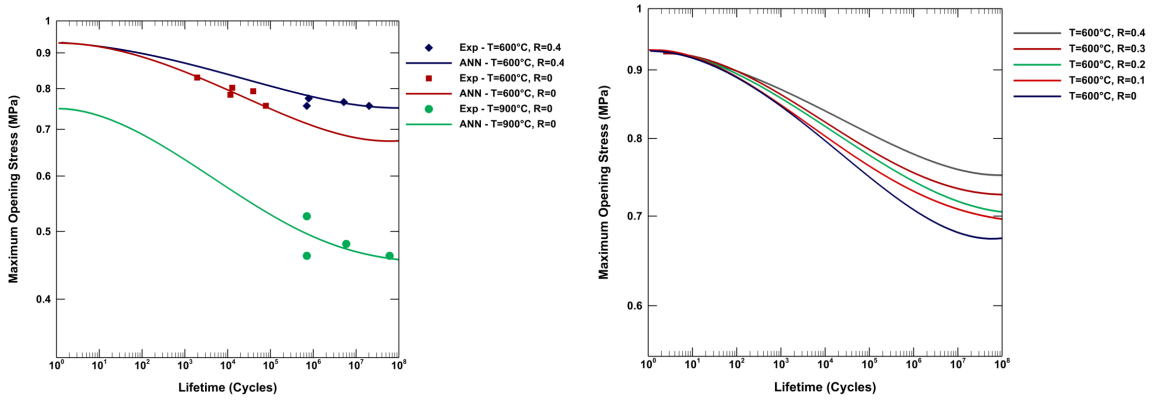

(**a**) (**b**)

Figure 11. Fatigue curves produced on training data spectrum for different temperatures and R ratios and their comparison with the experimental data (**a**) and for different R ratios at the same temperature (**b**).

The ultimate tensile strength (UTS) of metals typically exhibits a slight decrease with increasing temperature due to thermal relaxation effects up to a certain threshold temperature. Beyond this threshold, a rapid and nonlinear decrease in UTS is commonly observed. For nickel-based superalloys, this threshold temperature is often around 500 °C to 600 °C, although it may vary depending on the alloy composition [34]. Prediction results between 600 °C and 900 °C exhibit coherent behavior with respect to temperature, in which ultimate tensile strength (UTS) and fatigue limit decrease with increasing temperature since the material becomes softer. Since the predictions presented in Figure 12 are above the threshold temperature, material properties like yield strength and UTS are considered significantly affected, leading to pronounced changes in fatigue behavior. In contrast, the predictions represented in Figure 11b for different R-ratios at the same temperature still start from the same UTS, as the initial lifetime is always defined as 1 cycle. This results in the temperature influence being more dominant in the low-cycle region. Since UTS and fatigue limit values are not provided to ANNs for 700 °C and 800 °C due to the characterization of these properties not being performed at these temperatures, real-life values may differ from the represented data in Figure 12. However, this difference can be overcome by simply introducing the ANNs characterized fatigue limit and UTS values to further enhance the performance of the model.

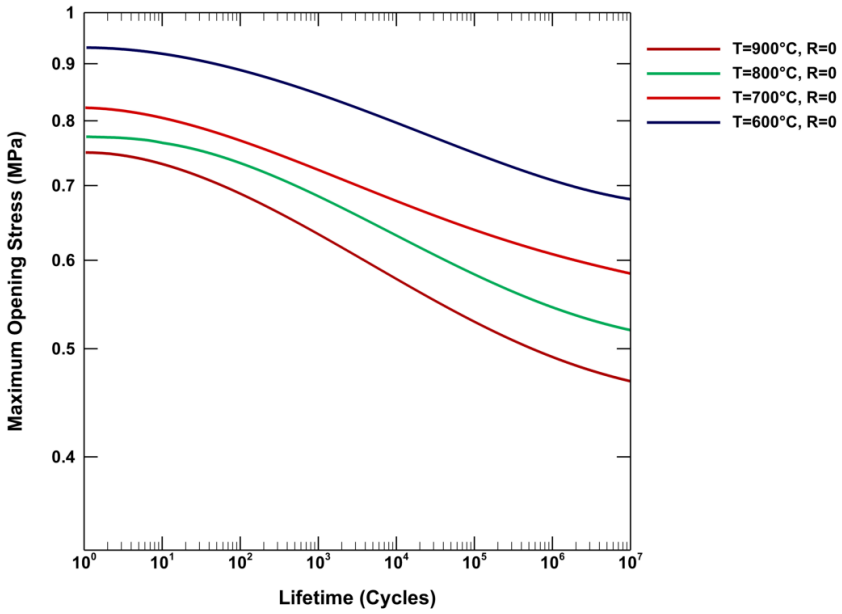

Figure 12. Fatigue curves prediction at various temperatures for CMSX-4.

4. Conclusions

In this study, the damage-based lifetime prediction model presented by Chaboche and Lemaitre is modified as an anisotropic lifetime assessment model by considering Mode I crack opening stress to predict the effect of anisotropy on single crystal component lives. This lifetime assessment model is combined with the rate-dependent crystal plasticity model presented in Section 2.2 to achieve the octahedral and cubic slip system behaviour of FCC single crystals.

HCF lifetime estimation of Ni-based single crystal CMSX-4 for a notched specimen at 750 °C for different R ratios is in good agreement with the experimental data. In addition, crack initiation locations are predicted for different crystal orientations of the notched specimen, showing coherent results with the fatigue tests conducted on another Ni-based

single crystal SC16 specimen. This proves that the model is coherent in estimating both lifetime values and crack initiation points of geometries with stress concentration zones.

Choosing cleavage stress as the critical stress for lifetime estimation considers both crack initiation and propagation contributions to the life of the specimen, even under fast crack propagation loadings and life HCF loadings. These results show that it is possible to achieve correct predictions for real-life geometries, like turbine blades, under both creep and combined fatigue loadings since cleavage systems are more apparent under LCF loadings. Further modifications, such as creep–fatigue interaction (which has already been developed by Chaboche [16]) and HCF-LCF superimposition, are required for the modified Chaboche model presented in this paper to predict real-life single crystal components with complex geometries.

ANNs achieve accurate predictions with low uncertainty for small and moderate perturbations. At 5% perturbation, the average multiplicative uncertainty of approximately 3.5 is acceptable for fatigue lifetime predictions, supported by strong performance metrics with R^2 values above 0.99 and MAE near 0.15 on both validation and test datasets.

While the parameters of the modified damage model are inherently temperature-dependent, necessitating careful optimization for each specific temperature condition, ANNs present a robust alternative for predicting fatigue curves across varying temperatures. The research highlighted that with a sufficient dataset, ANNs could effectively internalize and replicate the complex behaviors captured by the damage model, adapting to different thermal environments without the need for manual re-parameterization. This capability not only streamlines the predictive process but also enhances the scalability of fatigue life assessments in practical engineering applications.

Integrating ANNs with traditional damage models like the Chaboche damage model could significantly improve the efficiency and accuracy of lifetime predictions for critical components under diverse operational stresses and temperatures. Provided fatigue tests with dwell times and HCF-LCF combinations, wide-range lifetime predictions with ANNs for such loading conditions seem attainable.

Author Contributions: Conceptualization, O.A.; methodology (crystal plasticity), Ç.K.; methodology (lifetime assessment modeling), U.K.; validation, U.K.; writing—original draft preparation, U.K.; writing—review and editing, all of the authors; visualization, U.K.; supervision, O.A.; funding acquisition, Ç.K. All authors have read and agreed to the published version of the manuscript.

Funding: This research was funded by the TÜBİTAK 2244 Industrial PhD Program under project number [119C037]. Additionally, publication fees were covered by Turkish Aerospace Industries (TAI).

Institutional Review Board Statement: Not applicable.

Informed Consent Statement: Not applicable.

Data Availability Statement: Restrictions apply to the availability of these data. Data were obtained from the PREMECCY project (Contract number: AST5-CT-2006-030889) and are available from the author, Ozgur Aslan, with the permission of the PREMECCY project.

Acknowledgments: The author(s) would like to acknowledge the financial support provided by TÜBİTAK through the 2244 Industrial PhD Program. Special thanks to TUSAŞ Engine Industries (TEI) for their collaboration and contribution to this program. The support from all institutions has been instrumental in conducting this research.

Conflicts of Interest: Author Çağatay Kasar was employed by the company Turkish Aerospace Industries, Inc. (TAI). The remaining authors declare that the research was conducted in the absence of any commercial or financial relationships that could be construed as a potential conflict of interest.

References

1. Shi, Z.; Wang, X.; Liu, S.; Li, J. Low cycle fatigue properties and microstructure evolution at 760 °C of a single crystal superalloy. *Prog. Nat. Sci. Mater. Int.* **2015**, *25*, 78–83. https://doi.org/10.1016/j.pnsc.2015.01.009.
2. Wang, R.; Zhang, B.; Hu, D.; Jiang, K.; Hao, X.; Mao, J.; Jing, F. In-phase thermomechanical fatigue lifetime prediction of nickel-based single crystal superalloys from smooth specimens to notched specimens based on coupling damage on critical plane. *Int. J. Fatigue* **2019**, *126*, 327–334. https://doi.org/10.1016/j.ijfatigue.2019.05.003.
3. Riccius, J.; Zametaev, E. HCF and LCF Analysis of a Generic Full Admission Turbine Blade. *Aerospace* **2023**, *10*, 154. https://doi.org/10.3390/aerospace10020154.
4. Hou, J.; Wicks, B.J.; Antoniou, R.A. An investigation of fatigue failures of turbine blades in a gas turbine engine by mechanical analysis. *Eng. Fail. Anal.* **2002**, *9*, 201–211.
5. Kalluri, S.; McGaw, M.A. Effect of Tensile Mean Stress on Fatigue Behavior of Single-Crystal and Directionally Solidified Superalloys. In Proceedings of the Symposium on Cyclic Deformation, Fracture, and Nondestructive Evaluation of Advanced Materials, San Antonio, TX , USA, 12–13 November 1990.
6. Arakere, N.K.; Swanson, G. Effect of crystal orientation on fatigue failure of single crystal nickel base turbine blade superalloys. *J. Eng. Gas Turbines Power* **2002**, *124*, 161–176. https://doi.org/10.1115/1.1413767.
7. Hong, H.U.; Kang, J.G.; Choi, B.G.; Kim, I.S.; Yoo, Y.S.; Jo, C.Y. A comparative study on thermomechanical and low cycle fatigue failures of a single crystal nickel-based superalloy. *Int. J. Fatigue* **2011**, *33*, 1592–1599. https://doi.org/10.1016/j.ijfatigue.2011.07.009.
8. Okazaki, M.; Sakaguchi, M. Thermo-mechanical fatigue failure of a single crystal Ni-based superalloy. *Int. J. Fatigue* **2008**, *30*, 318–323. https://doi.org/10.1016/j.ijfatigue.2007.01.044.
9. Yu, Y.; Zhu, S.P.; Liu, Q.; Liu, Y. A new energy-critical plane damage parameter for multiaxial fatigue life prediction of turbine blades. *Materials* **2017**, *10*, 513. https://doi.org/10.3390/ma10050513.
10. Aslan, O. Numerical Modeling of Fatigue Crack Growth in Single Crystal Nickel-Based Superalloys. Ph.D. Dissertation, Ecole Nationale Supérieure des Mines de Paris, Paris, France, 2010.
11. Aslan, O.; Bayraktar, E. A Large-Deformation Gradient Damage Model for Single Crystals Based on Microdamage Theory. *Appl. Sci.* **2020**, *10*, 9142. https://doi.org/10.3390/app10249142.
12. Brown, M.W.; Miller, K.J. A theory for fatigue failure under multiaxial stress-strain conditions. *Proc. Inst. Mech. Eng.* **1973**, *187*, 745.
13. Bourbita, F.; Rémy, L. A combined critical distance and energy density model to predict high temperature fatigue life in notched single crystal superalloy members. *Int. J. Fatigue* **2016**, *84*, 17–27. https://doi.org/10.1016/j.ijfatigue.2015.11.007.
14. Levkovitch, V.; Sievert, R.; Svendsen, B. Simulation of deformation and lifetime behavior of a fcc single crystal superalloy at high temperature under low-cycle fatigue loading. *Int. J. Fatigue* **2006**, *28*, 1791–1802. https://doi.org/10.1016/j.ijfatigue.2005.12.006.
15. Santecchia, E.; Hamouda, A.M.S.; Musharavati, F.; Zalnezhad, E.; Cabibbo, M.; El Mehtedi, M.; Spigarelli, S. A Review on Fatigue Life Prediction Methods for Metals. *Adv. Mater. Sci. Eng.* **2016**, *2016*, 1–26. https://doi.org/10.1155/2016/9573524.
16. Chaboche, J.L.; Lemaitre, J. *Mechanics of Solid Materials*; Cambridge University Press: Cambridge, UK, 1990.
17. Zhang, B.; Wang, R.; Hu, D.; Jiang, K.; Hao, X.; Mao, J.; Jing, F. Damage-based low cycle fatigue lifetime prediction of nickel-based single crystal superalloy considering anisotropy and dwell types. *Fatigue Fract. Eng. Mater. Struct.* **2020**, *43*, 2970–2983. https://doi.org/10.1111/ffe.13345.
18. Samavatian, V.; Fotuhi-Firuzabad, M.; Samavatian, M.; Dehghanian, P.; Blaabjerg, F. Correlation-driven machine learning for accelerated reliability assessment of solder joints in electronics. *Sci. Rep.* **2020**, *10*, 14821. https://doi.org/10.1038/s41598-020-71926-7.
19. George, A.; Zipprich, J.; Breitenbach, M.; Klingler, M.; Nowottnick, M. Reliability investigation of large area solder joints in power electronics modules and its simulative representation. *Microelectron. Reliab.* **2018**, *88–90*, 762–767. https://doi.org/10.1016/j.microrel.2018.06.049.
20. Cailletaud, G. Une Approche Micromécanique Phénoménologique du Comportement inéLastique des méTaux. Ph.D. Dissertation, Paris 6-Jussieu, Paris, France, 1987.
21. Castelluccio, G.M.; McDowell, D.L. Mesoscale cyclic crystal plasticity with dislocation substructures. *Int. J. Plast.* **2017**, *98*, 1–26.
22. Clayton, J.D. *Nonlinear Mechanics of Crystals*; Springer: Dordrecht, The Netherlands, 2011; pp. 558–559. https://doi.org/10.1007/978-94-007-0350-6.
23. Meric, L.; Poubanne, P.; Cailletaud, G. Single Crystal Modeling for Structural Calculations: Part 1-Model Presentation. *Eng. Mater. Technol.* **1991**, *113*, 162–170.
24. Donahue, R.J.; Clark, H.M.; Atanmo, P.; Kumble, R.; McEvily, A.J. Crack Opening Displacement and The Rate of Fatigue Crack Growth. *Int. J. Fract. Mech.* **1972**, *8*, 209–219.
25. Hoshidet, T.; Socies, D.F. Mechanics of mixed mode small fatigue crack growth. *Eng. Fract. Mech.* **1987**, *26*, 841–850.

26. Lankford, J.; Davidson, D.L.; Chan, K.S. The Influence of Crack Tip Plasticity in the Growth of Small Fatigue Cracks. *Metall. Mater. Trans. A* **1984**, *15*, 1579–1588.
27. Qian, J.; Fatemi, A. Mixed mode fatigue crack growth: A literature survey. *Eng. Fract. Mech.* **1996**, *55*, 969–990.
28. Montesinos López, O.A.; Montesinos López, A.; Crossa, J. Fundamentals of Artificial Neural Networks and Deep Learning. In *Multivariate Statistical Machine Learning Methods for Genomic Prediction*; Springer International Publishing: Cham, Switzerland, 2022; pp. 379–425. https://doi.org/10.1007/978-3-030-89010-0_10.
29. Niazi, M.S.; Wisselink, H.H.; Meinders, T. Viscoplastic regularization of local damage models: Revisited. *Comput. Mech.* **2012**, *51*, 203–216. https://doi.org/10.1007/s00466-012-0717-7.
30. Henann, D.L.; Anand, L. A large deformation theory for rate-dependent elastic-plastic materials with combined isotropic and kinematic hardening. *Int. J. Plast.* **2009**, *25*, 1833–1878. https://doi.org/10.1016/j.ijplas.2008.11.008.
31. Dye, D.; Coakley, J.; Vorontsov, V.A.; Stone, H.J.; Rogge, R.B. Elastic moduli and load partitioning in a single-crystal nickel superalloy. *Scr. Mater.* **2009**, *61*, 109–112. https://doi.org/10.1016/j.scriptamat.2009.03.008.
32. Sengupta, A.; Putatunda, S.K.; Bartosiewicz, L.; Hangas, J.; Nailos, P.; Peputapeck, M.; Alberts, E.E. Tensile Behavior of a New Single-Crystal Nickel-Based Superalloy (CMSX-4) at Room and Elevated Temperatures. *J. Mater. Eng. Perform.* **1994**, *3*, 73–81.
33. Forest, S. Nickel base single crystals across length scales. In *Crystal Plasticity and Damage at Cracks and Notches in Nickel-Base Single-Crystal Superalloys*; Springer: Cham, Switzerland, 2022; pp. 457–473.
34. Tai, W.; Zhang, R.; Zhou, Z.; Cui, C.; Zhou, Y.; Sun, X. Tensile Properties and Deformation Mechanisms of Ni–Co–W Based Superalloy with High γ' Content. *Met. Mater. Int.* **2024**, *30*, 2397–2405. https://doi.org/10.1007/s12540-024-01647-3.